Available online at www.sciencedirect.com

ScienceDirect

Advances in Space Research xxx (xxxx) xxx

ADVANCES IN SPACE RESEARCH (a COSPAR publication)

www.elsevier.com/locate/asr

Unsupervised band selection based on covariance matrix for hyperspectral image classification

Eman N. Abdelhafez [a], Ahmed Hagag [a,b,*], Tamer A. Abassy [a]

[a] Department of Scientific Computing, Faculty of Computers and Artificial Intelligence, Benha University, Benha 13518, Egypt
[b] Information Technology and Computing Program, Faculty of Computer Studies, Arab Open University, Egypt

Received 22 July 2025; received in revised form 25 September 2025; accepted 9 October 2025

Abstract

Although spectral–spatial classification in hyperspectral imagery (HSI) delivers high accuracy, it remains sensitive to noise and redundant information in raw spectral bands. To address this issue, we propose a novel unsupervised band selection method for hyperspectral image classification. The approach begins with spectral band analysis, followed using a covariance matrix to identify and retain the most informative bands. A deep convolutional neural network (CNN) is then applied to the selected bands to extract global features, which are subsequently classified using both SoftMax and support vector machine (SVM) classifiers. We validated the effectiveness of our method on the Indian Pines and Salinas-A datasets, achieving accuracies of 97.66 % and 97.91 %, representing improvements of 4 % and 2.21 %, respectively. These results demonstrate that our method significantly outperforms existing approaches in terms of classification accuracy.

Keywords: Hyperspectral image classification; Band selection; Covariance matrix; Convolution neural network

1. Introduction

A collection of many narrow-band images covering a broad spectral range is called a hyperspectral image (HSI). The same scene, made up of various objects taken at different wavelengths, is reflected in each band; the spatial information, however, is largely stable among bands. It is possible to use both spectral and spatial information to identify and categorize things (Patro et al., 2021). In environmental and agricultural monitoring, it reveals subtle biochemical and structural features of vegetation, soil, and water enabling early detection of crop diseases, nutrient deficiencies, soil properties, and water pollutants (Lowe et al., 2017, Lu et al., 2020, Stuart et al., 2019, Vairavan et al., 2024). HSI, along with multispectral and thermal imaging, provides comprehensive information for diverse applications. In medicine, HSI supports non-invasive melanoma detection and skin diagnostics by capturing detailed spectral data (Jia et al., 2021). In the military domain, HSI significantly enhances surveillance and reconnaissance by detecting camouflaged targets, distinguishing materials, and supporting unmanned aerial vehicle (UAV)-based workflows for ordnance and hazard detection. Collectively, these applications demonstrate HSI's value as a non-invasive, precise, and versatile technology for both civilian and military domains (Eckel and Stütz, 2024, Zhao et al., 2022). Current research focuses on hyperspectral image classification, aiming to address

* Corresponding author at: Department of Scientific Computing, Faculty of Computers and Artificial Intelligence, Benha University, Benha 13518, Egypt.
E-mail addresses: eman.elsayed@fci.bu.edu.eg (E.N. Abdelhafez), ahagag88@gmail.com, ahagag@fci.bu.edu.eg, a.hagag@aou.edu.eg (A. Hagag), tamerabassy@yahoo.com (T.A. Abassy).

https://doi.org/10.1016/j.asr.2025.10.036

Please cite this article as: E. N. Abdelhafez, A. Hagag and T. A. Abassy, Unsupervised band selection based on covariance matrix for hyperspectral image classification, Advances in Space Research, https://doi.org/10.1016/j.asr.2025.10.036

high-dimensional challenges. Two main approaches are being explored: dimensionality reduction of hyperspectral data and augmenting classifier processing capabilities with high-dimensional features. These strategies seek to enhance the efficiency and accuracy of hyperspectral image classification methods (Sun and Du, 2019, Hamida et al., 2018, Shawky et al., 2020, Mohammad et al., 2024). Dimensionality reduction in hyperspectral data can be accomplished via band selection or feature extraction techniques. Meanwhile, diminishing the computational load of classifiers using high-dimensional features can be achieved through methods such as linear discriminant analysis and principal component analysis. These approaches play crucial roles in streamlining hyperspectral data analysis and classification processes (Hamida et al., 2018). Band selection in remote sensing entails strategic elimination of spectral bands based on sensor characteristics and data quality. Problematic bands, such as those affected by water absorption or low signal-to-noise ratios, are often excluded to enhance data integrity. This process not only improves classifier robustness but also mitigates the curse of dimensionality, a phenomenon where classification performance diminishes with increasing data dimensions. Techniques like principal component analysis (PCA) and mutual information aid in identifying and discarding redundant or uninformative bands. However, careful consideration is essential as unsupervised dimension reduction methods may inadvertently remove discriminative information crucial for classification accuracy. Balancing dimensionality reduction with preservation of discriminative features is crucial for optimal band selection. Moreover, band selection plays a pivotal role in enhancing the efficiency and efficacy of remote sensing data analysis pipelines (Patro et al., 2021, Li et al., 2021, Audebert et al., 2019).

Recently, image analysis for remote sensing has become increasingly focused on methods based on deep learning. Audebert et al. (2019) discussed machine learning methods for hyperspectral classification, addressing challenges like spatial and spectral resolution, data volume, and model transfer from multimedia images. In (Wang et al., 2021) pioneering classification framework titled spatial-spectral transformer (SST) was unveiled for HSI classification, incorporating deep convolutional neural network (CNN), modified Transformer, multilayer perceptron, dynamic feature augmentation, transfer learning, and label smoothing. Wang et al. (2023) developed adaptive multiscale multimodal network (AMM-Net), a deep network that enhances classification accuracy by combining spatial and spectral feature extraction modules. In (Torun et al., 2024) introduced self-modulating CNN (SM-CNN), a self-modulating convolutional neural network utilizing correlated spectral and spatial information with a spectral self-modulating residual block for improved noise handling.

The research gap shows that related works have not sufficiently emphasized band selection as a strategy for reducing redundancy and noise in hyperspectral data. Therefore, our first objective is to propose an effective band selection method that reduces the number of bands by removing less informative ones. The second objective is to develop a CNN-based classification model that leverages the refined spectral-spatial information to improve classification accuracy. Most related deep-learning models aim to improve classification accuracy. However, there is a need to reduce bands of image. As a result of this, we used the band selection method to create a novel classification framework for HSI images in this work. The primary contributions outlined in this paper encompass:

- We propose an unsupervised band selection technique that utilizes the absolute spectral wavelet differences between classes, along with a covariance matrix, to isolate the most relevant bands. This process minimizes redundancy, accelerates computation, and enhances classification accuracy.
- A CNN is designed to capture discriminative spatial–spectral features from the reduced band set. For final classification, both SoftMax and support vector machine (SVM) methods are applied, ensuring strong predictive performance across classes.
- The effectiveness of the proposed framework is verified through extensive testing on two benchmark hyperspectral datasets. The findings demonstrate notable gains in accuracy and efficiency, confirming the practicality and robustness of the approach for hyperspectral image classification.

The subsequent sections of this paper are structured as follows: Section 2 offers an overview of existing research on HSI image classification. Section 3 introduces our proposed methodology, detailing each component. Following that, Section 4 discusses the dataset, experimental setup, and results. Finally, Section 5 concludes with a summary of findings and suggestions for future research directions.

2. Related work

In current literature, considerable attention has been devoted to the classification of satellite hyperspectral images, Audebert et al. (2019) provide a comprehensive overview of previous machine-learning methodologies, assess a range of deep learning techniques proposed for hyperspectral classification, and pinpoint the challenges encountered when deploying deep neural networks for this purpose. Specifically, they delve into issues surrounding spatial and spectral resolution, data volume management, and the transferability of models from multimedia images to hyperspectral data. Zhao et al. (2020) have devised a band selection method aimed at identifying crucial bands, which is then integrated into the conditional random field–based band selection (CRFBS) algorithm to mitigate the impact of noisy bands. Their approach leverages both spectral and spatial cues to enhance the overall classification performance. The selection of bands is guided by the assessment of their relative utility in the classification

process. The study in (Mou et al., 2021) utilizes deep reinforcement learning for unsupervised hyperspectral band selection, introducing a specialized Markov decision process parameterization. The method designs tailored actions, states, and environment simulations, with two reward scheme variations. A deep Q-network is trained to learn an optimal band-selection policy, validated across diverse datasets and classifiers, showcasing its robustness. The study in (Wang et al., 2021) introduced the SST, was introduced for HSI classification. This framework comprises various elements: a CNN for extracting spatial features, an adapted Transformer model for capturing sequential spectral dependencies, and a multilayer perceptron for classification purposes. Furthermore, dynamic feature augmentation is integrated to combat overfitting and improve the model's generalization ability. Transfer learning is also utilized within SST to handle situations with limited training data, and label smoothing is introduced specifically for T-SST-based classification.

Recently, Li et al. (Huang et al., 2023) introduced three innovative units—FCTN-FC, FCTNConv2D, and FCTNConv3D—aimed at compressing the weight tensor of standard fully connected (FC) layers and the kernel tensor of convolutional layers. Their model, HybridFCTCN, incorporates a hybrid architecture for spatial-spectral feature learning. Initially, FCTNConv3D was employed for preprocessing, followed by spatial feature enhancement using FCTNConv2D. This approach allows the model to acquire highly discriminative features while maintaining a lightweight network architecture, thus addressing overfitting concerns, particularly in scenarios with limited sample sizes. The proposed model achieves state-of-the-art classification performance, showcasing its effectiveness in practical applications. Furthermore, Li et al. analyze the rank of FCTND-based units and discusses rank determination across different layers of HybridFCTCN, facilitating its implementation. The study in (Wang and Liang, 2023) introduced a hybrid network model (HNM), employing a lightweight 3D-M convolution network and scalable graph convolutional network (GCN). This model effectively captures spectral-spatial features from HIS while keeping computational complexity to a minimum. Wang et al. (2023) presented the Attention Mechanism and multigroup strategy network (AMM-Net), a deep learning model that integrates spatial and spectral feature extraction components to improve classification accuracy using 500 epoch. The spatial feature extraction incorporates the channel spatial attention module (CSAM) to emphasize relevant features for classification, whereas the spectral feature extraction module utilizes a long- and short-term memory (LSTM) network to thoroughly analyze spectral information. Evaluation of the AMM-Net on three benchmarks for HSI showcased impressive performance results. The study in (Torun et al., 2024) presented the self-modulating convolutional neural network (SM-CNN), a model designed to leverage correlated spectral and spatial information. Central to the architecture is the spectral self-modulating residual block (SSMRB), which dynamically adjusts features using neighboring spectral data, thereby enhancing noise handling capabilities. By integrating SSMRB, the denoising network transforms into a dynamic entity, enabling adaptive feature adjustments during the denoising process for each input HSI based on its distinct spatial-spectral characteristics. Javad et al. (Mahmoodi et al., 2024) proposed method integrates spectral and spatial attention for hyperspectral image classification. PCA reduces band redundancy, followed by an entropy-based module to enhance informative features. A hybrid network combining 3D and 2D CNNs with skip connections, along with depth wise spatial attention and reshape softmax spectral attention, captures essential spatial–spectral information while reducing complexity. The study (Sharifi and Safari, 2025) proposed a transformer-based deep learning model to enhance the spatial resolution of Sentinel-2 images using multihead, spatial, and channel attention. Evaluated on Sentinel-2, AID, and UC-Merced datasets, the model achieved superior performance with PSNR of 33.52 dB, SSIM of 0.862, and SRE of 36.7 dB. The study (Hu et al., 2025) proposed a new band selection method for hyperspectral images based on global partition clustering. Unlike traditional methods that rely on fixed partitions and often produce redundant bands, this approach uses similarity-based structural ranking to more effectively divide the band space and select representative bands. It considers the relationship between the total and selected bands to reduce redundancy and improve selection quality. In (Vafaeinejad et al., 2025), the authors proposed a method that leverages the segment anything model (SAM) to achieve 92 % classification accuracy, 40 % faster processing, and full automation in land mapping. Their approach demonstrated significant improvements in agricultural boundary delineation, land-use planning, and dispute resolution, while also reducing environmental impacts. As a scalable and open-source solution, the method modernizes cadastral mapping practices, contributing to enhanced efficiency and sustainability.

Table 1 presents an overview of the outcomes derived from various studies focusing on the classification of HSI data. Consequently, we propose a selective band approach to benchmark the Indian Pine and Salinas datasets, achieving optimal diagnostic accuracy.

3. Methodology

In this study, we introduce an unsupervised band selection approach for HSI classification. The overall framework of the proposed model is depicted in Fig. 1. First, we provide a description of the HSI datasets used in the experiments. Next, the band selection method is applied to reduce data dimensionality by identifying a subset of the most informative bands. The reduced data is then processed by a deep CNN to extract global spatial–spectral

Table 1
Overview of previous research efforts in HSI classification.

Study	Method Used and Training Model	Dataset(s)	Training Ratio	Accuracy	Limitation
Audebert et al. (Audebert et al., 2019)	3D CNN	Indian pines	20 %	75.47 %	Low Accuracy
Zhao et al. (Zhao et al., 2020)	CRFBS	Indian pines	7 %	88.64 %	Non-Data Preprocessing
		Salinas		92.56 %	
Mou et al. (Mou et al., 2021)	DRL + SVM-RBF	Indian pines	10 %	74.39 %	Non-Data Preprocessing & Low Accuracy
Wang et al. (Wang et al., 2021)	T-SST-L	Indian pines	2 %	83.05 %	Non-Band Selection
		Salinas		96.08 %	
Huang et al. (Huang et al., 2023)	HybridFCTCN	Indian pines	10 %	87.62 %	Non-Band Selection
Wang and Liang (Wang and Liang, 2023)	HNM	Indian pines	10 %	95.26 %	Non-Band Selection & Non-Data Preprocessing
Wang et al. (Wang et al., 2023)	AMM–Net	Indian pines	10 %	96.05 %	Non-Band Selection
		Salinas		99.75 %	
Torun et al. (Torun et al., 2024)	SM-CNN	Indian pines	10 %	89.31 %	Non-Band Selection
Mahmoodi et al. (Mahmoodi et al., 2024)	DESSA-Net	Indian pines	10 %	85.62 %	Non-Band Selection
		Salinas-A		95.98 %	
Sharifi and Safari (Sharifi and Safari, 2025)		Indian pines	10 %	95.62 %	Non-Band Selection
	Sentinel-2	Salinas-A		96.36 %	
Hu et al. (Hu et al., 2025)	GPCBS	Indian pines	10 %	72.48 %	Non-Data Preprocessing
		Salinas		87.18 %	

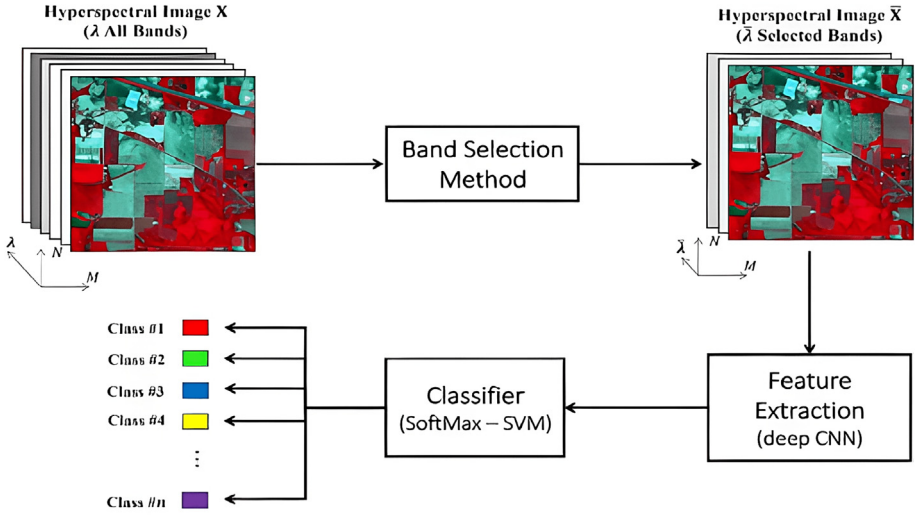

Fig. 1. Framework of the proposed model, which integrates band selection to enhance HSI classification.

features. Finally, classification is performed using both SoftMax and SVM classifiers. Detailed explanations of each stage of the framework are presented in the following sections.

3.1. Description of datasets

High-resolution satellite images offer full information about objects like homes, plants, and cars. It is suggested to use a deep hierarchical representation to fully characterize these images. Basic elements such as roads, forests, and lakes are delineated by distinct combinations, whereas elemental vectors delineate attributes like color, texture, and shape. However, isolated objects alone fail to capture the holistic scene or its underlying significance owing to their spatial and spectral proximity. Hence, to extract meaningful insights, spatial interactions must be incorporated at a higher level of the representation hierarchy. This will show semantic rules that identify high-level semantic classes (Hamida et al., 2018). Two benchmark datasets for HSI classification were used:

1) Indian Pines Dataset:

Collected by the AVIRIS sensor over the Indian Pines test site in northwestern Indiana, USA. It consists of 224 spectral bands in the wavelength range of 0.4–2.5 μm, with

a spatial resolution of 20 m per pixel. After removing water absorption bands, typically 200 bands are retained. The image size is 145 × 145 pixels, and it contains 16 ground-truth classes, mainly representing agricultural crops, forests, and natural vegetation (Huang et al., 2023).

2) Salinas-A Dataset:

Acquired by the AVIRIS sensor over the Salinas Valley, California, USA. It is a small subscene (a subset of the larger Salinas dataset) with an image size of 86 × 83 pixels and 224 spectral bands in the range of 0.4–2.5 μm. After removing water absorption bands, 204 bands are typically used. The dataset contains 6 ground-truth classes, mostly vegetables, bare soils, and vineyard fields (Ahishali et al., 2022).

The specifics of the selected datasets are outlined in Table 2. Moreover, Fig. 2 shows the dataset Indian Pines Scene for each class, and Fig. 3 shows the dataset Salinas-A Scene for each class. Two datasets were employed to facilitate benchmarking and comparison.

3.2. Band selection method

The band selection process begins with a detailed analysis of wavelength attributes across the individual classes of the Indian Pines dataset, capturing key spectral characteristics that differentiate various land cover categories. An unsupervised band selection algorithm is then employed to automatically determine the most informative subset of bands. The primary objectives of this process are to remove redundant or noisy spectral information that may hinder classification accuracy, and to enhance computational efficiency by reducing the dimensionality of hyperspectral data while preserving class-discriminative features. The subsequent methodology section outlines

Table 2
Key information on the benchmark HSI datasets.

Dataset	Pixels	Classes	Image size	Num of Bands	Spatial resolution (*m*)	spectral bands (μ*m*)
Indian Pines Scene	10,249	16	145 × 145	200	20	0.4 to 2.5
Salinas-A	5348	6	86 × 83	204	3.7	0.4 to 2.5

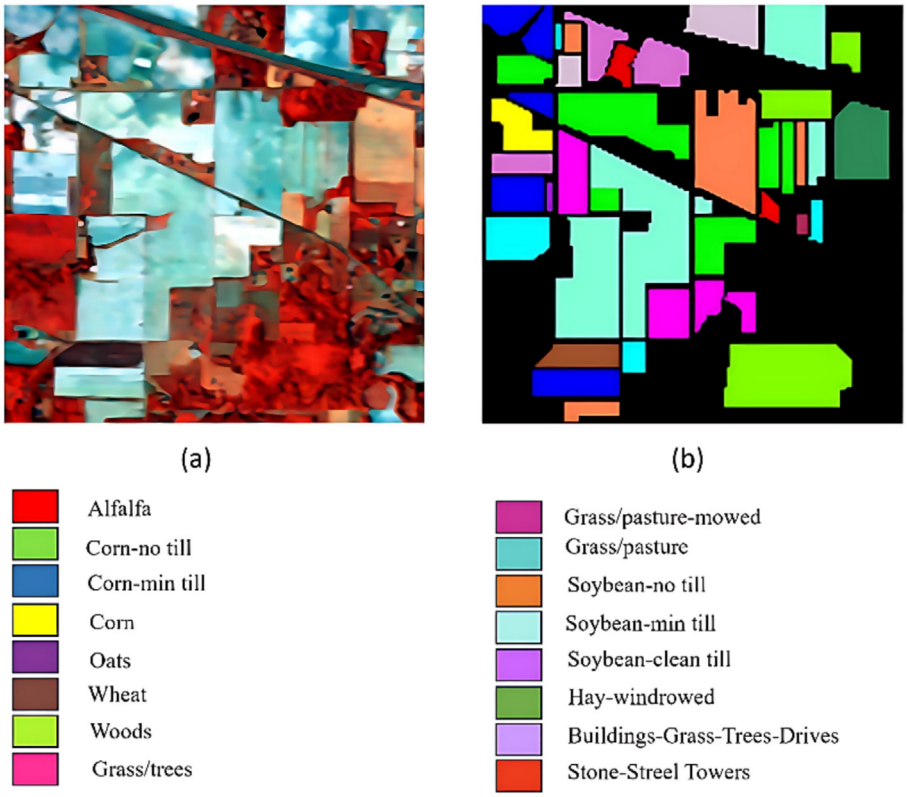

Fig. 2. Indian Pines dataset. (a) Three-band false color image. (b) Ground-truth image.

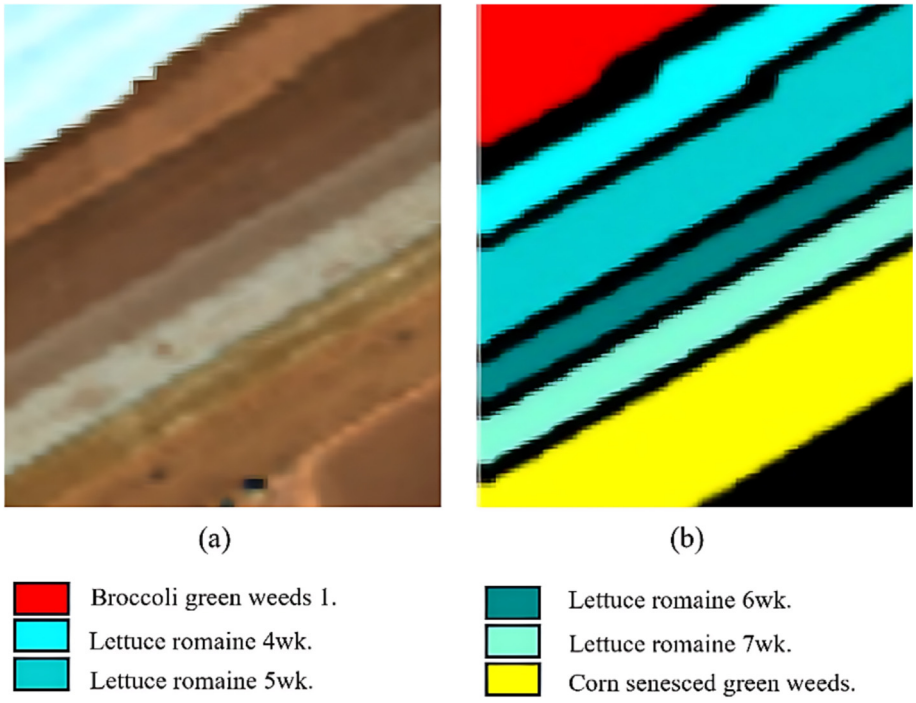

Fig. 3. Salinas-A dataset. (a) Three-band false color image. (b) Ground-truth image.

each step of the inspection and selection procedure, followed by a visual presentation of the selected bands, highlighting their significance in hyperspectral image analysis.

3.2.1. Spectral band analysis

Fig. 4 illustrates the average spectral signatures of all classes within the Indian Pines hyperspectral dataset. In this plot, each curve represents the mean spectral reflectance profile of pixels associated with a specific land-cover class, captured across the full spectral range. The x-axis corresponds to the wavelength or band index, reflecting the different spectral regions from visible to shortwave infrared, while the y-axis indicates the average reflectance intensity for each class. By analyzing these spectral curves, one can observe distinct absorption and reflectance patterns that characterize individual classes, such as vegetation, soil, and man-made structures. The noticeable differences in curve shapes and amplitudes highlight class-specific spectral features, which are critical for distinguishing between spectral categories. Moreover, this visualization not only underscores inter-class variability but also provides insight into intra-class consistency, as averaging reduces pixel-level noise while preserving class-specific patterns. Such spectral signature analysis forms the foundation of hyperspectral image classification, as it directly links spectral responses to material properties. Therefore, the figure serves as an essential reference for identifying discriminative bands, guiding band selection, and improving the interpretability of classification results in remote sensing applications.

3.2.2. Steps of the band selection algorithm

The proposed band selection method is illustrated in Algorithm 1. The HSI image is represented as a three-dimensional data cube, denoted as $\mathbf{X} \in \mathbb{R}^{H\times W\times C}$, where $\mathbf{X}$ represents the original HSI image. Here, H, W, and C denote the dimensions of height, width, and the count of spectral bands, respectively. The first step of the algorithm initializes two parameters, p_1 and p_2, which control the number of selected bands in different stages of the process. The average spectra AV of the classes are computed, followed by calculating the absolute difference between them to highlight the most distinctive spectral responses among classes, storing the results in the array *Subtracted classes*.

$$Subtracted\ classes[i] = |AV[i] - AV[j]| \tag{1}$$

The index of the maximum value in the *Subtracted classes* array is determined and stored in the variable *max_position*.

$$max\_position = argmaxi\ (Subtracted\ classes[i])) \tag{2}$$

The algorithm selects the first set of bands based on the indices up to p_1 from the *max_position* array. The frequency of each index in the first selected bands is counted, and the results are stored in frequency_index. The indices in *frequence_index* are sorted in increasing order to obtain some bands. *secondselection* are selected by taking the first p_2 elements from *frequence_index*. The original hyperspectral data cube $\mathbf{X}$ is updated to retain only the selected bands. The updated data cube $\mathbf{X}$ is standardized. Standard-

ization typically involves scaling the data to have zero mean and unit variance (Mishra et al., 2017). The formula for **X**_*Standardized* in the following equation.

$$\mathbf{X}\_Standardized = \sqrt{\frac{\sum_{i=1}^{n}(x-\mu)^2}{n}} \tag{3}$$

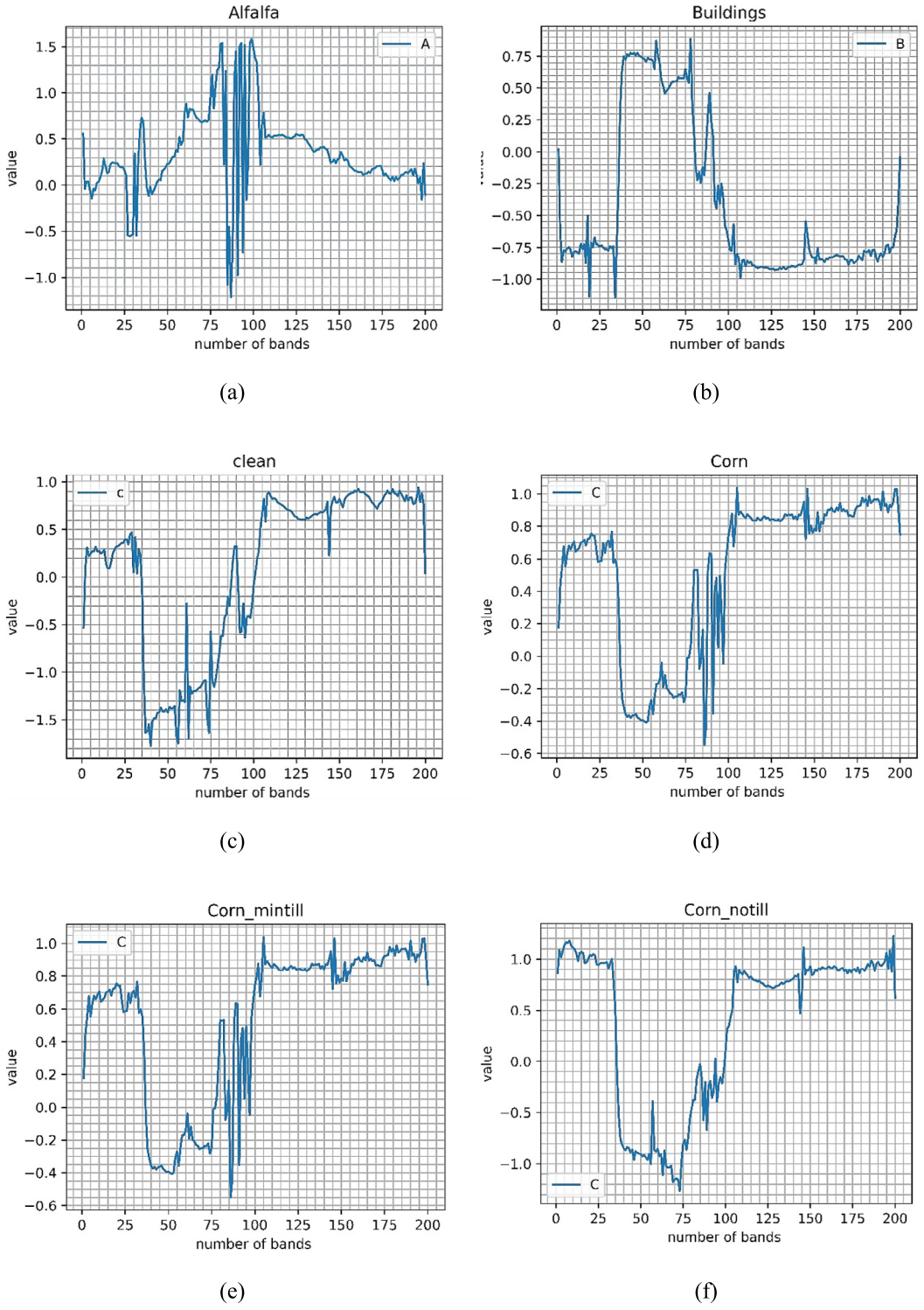

Fig. 4. Visualization of average spectral for each class on the Indian Pines dataset. (a) Alfalfa. (b) Buildings-Grass-Trees-Drivers. (c) Soybean-Clean. (d) Corn. (e) Corn-Mintill. (f) Corn-Notill. (g) Hay-Windrowed. (h) Grass-Pasture-Mowed. (i) Oats. (j) Grass-Pasture. (k) Soybean-Mintill. (l) Soybean-Notill. (m) Stone-Steel-Towers. (n) Grass-Trees. (o) Wheat. (p) Woods.

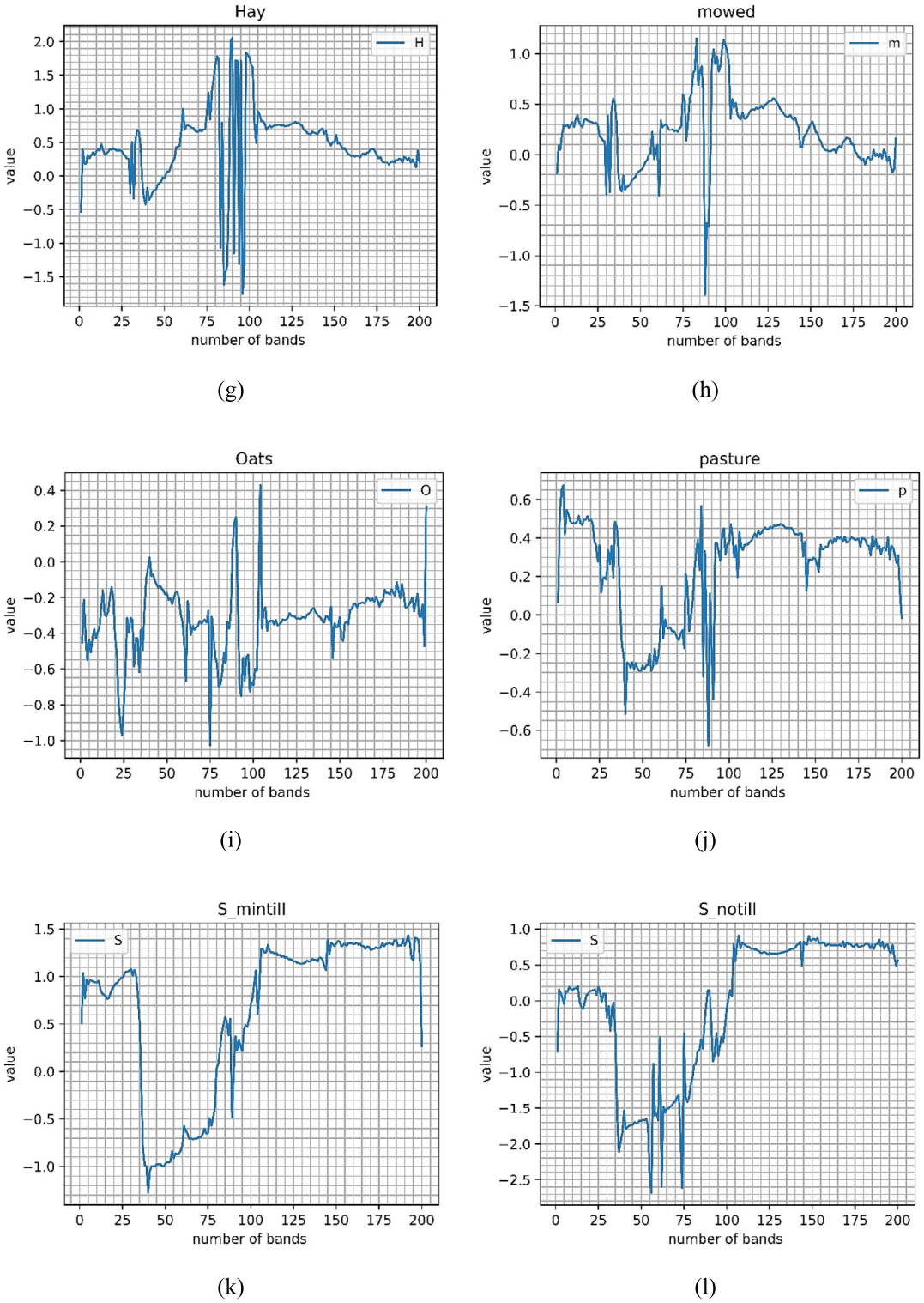

Fig 4. *(continued)*

where x is a value of band, μ is the mean of bands, and n is the number of bands. The *covariancematrix* of the standardized data is calculated.

$$covariance\,matrix = \frac{1}{n-1}\sum_{i=1}^{n}\left(x_i-\bar{x}\right)\left(y_i-\bar{y}\right) \tag{4}$$

where $\bar{x}$ and $\bar{y}$ are the arithmetic mean of x and y, respectively.

Some points to consider include that the diagonal elements represent the covariance values between each dimension with itself. Regarding *eigenvectors* and *eigenvalues*, the most common approach defines an *eigenvectors* of the

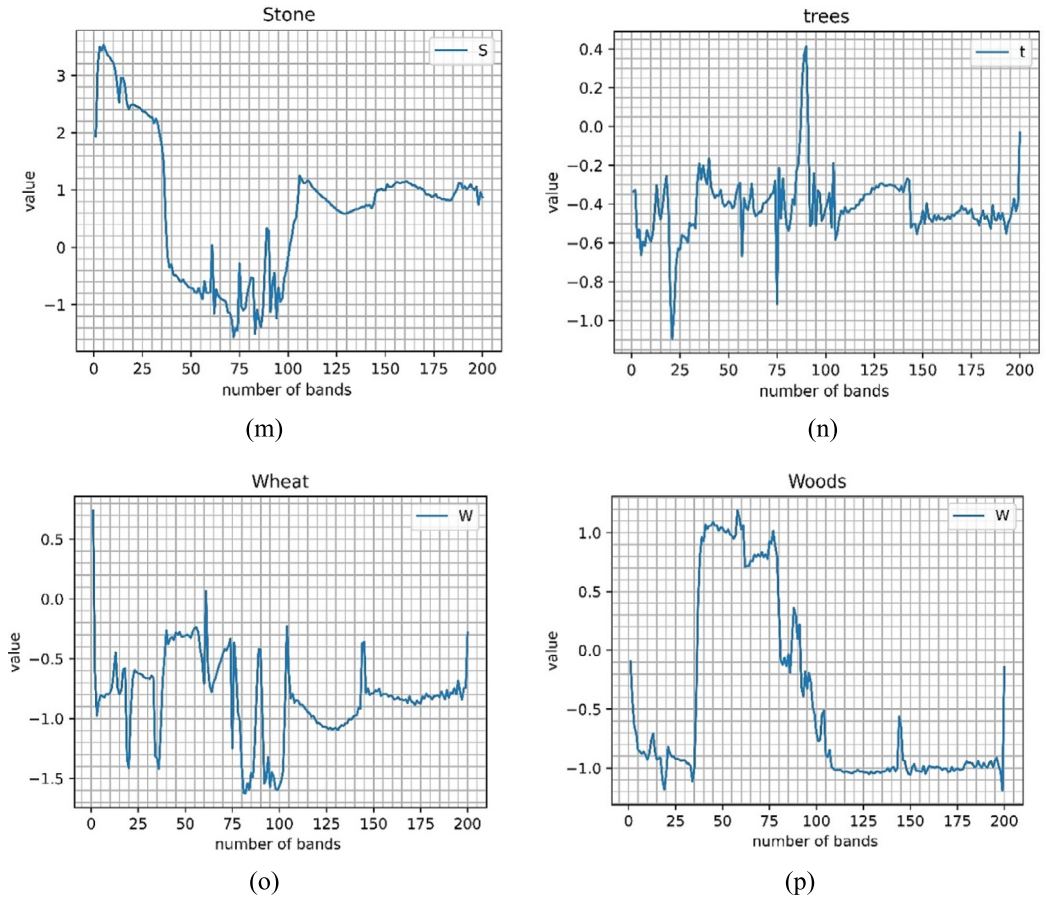

Fig 4. *(continued)*

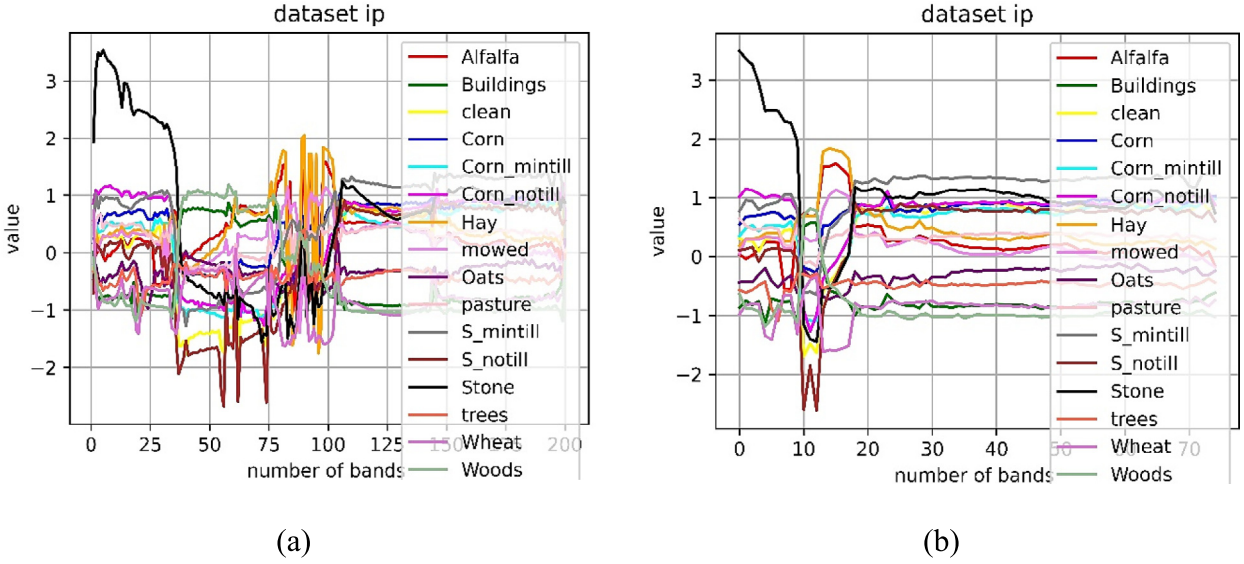

Fig. 5. Visualization of spectral bands on the Indian Pines dataset. (a) all bands, and (b) selected 75 bands.

covariancematrix as a vector u that satisfies the following equation.

$$covariancematrix.u = \lambda u \tag{5}$$

where, λ is a scalar called the *eigenvalues* associated to the *eigenvectors*.

The bands with maximum differences are prioritized, and frequency analysis ensures robust selection across multiple class comparisons. Finally, eigen-decomposition of the covariance matrix is performed to ensure that the selected bands capture the most informative variance, leading to the final subset.

$$selectedbands = \mathbf{X}\_Standardized\ .principalcomponents \quad (6)$$

where *principalcomponents* is the top Num components eigenvectors are selected. The final output of the algorithm is the *selectedbands*, representing a subset of bands considered relevant or important for further analysis. This approach combines spectral distinctiveness with statistical variance preservation, producing a band subset that balances interpretability, accuracy, and computational efficiency. Fig. 5 illustrates the output of the proposed band selection algorithm on the Indian Pines dataset. The method identifies and retains bands that exhibit the greatest spectral differences between classes, thereby selecting the most discriminative subset for classification.

Algorithm 1 (*Band Selection Based on Covariance Matrix*).

Input: HSI data cube **X**.
Output: Indices of bands selection.
Initialize first and second parameter number band p_1, p_2
Calculate Average bands of classes (*AV*).
While $i <$ length(*classes* – 1)
  While $j <$ length(*classes*)
    Subtracted classes[*i*] = abs (*AV* [*i*] - *AV* [*j*])
    Find the index of the maximum value in *Subtracted classes* and store it in *max_position*.
first selection= *max_position* [: p_1]
Count the frequency of each index in *first selection* to get *frequence_index*.
    Sort *frequence_index* in increasing order.
secondselection= *frequence_index* [: p_2]
X= **X**[: , *secondselection*]
X_*Standardized* = standardize (**X**)
covariancematrix= calculate_covariance_matrix (**X** _*Standardized*)
eigenvectors, *eigenvalues* = eigen decomposition (*covariancematrix*)
Sort the *eigenvectors* based on *eigenvalues* in descending order.
Select the top Num components *eigenvectors* *.principalcomponents*= sorted (*eigenvectors* [: :Num components])
selectedbands= **X** _*Standardized* **principalcomponents*
Return *selectedbands*

3.3. Feature extraction

Feature extraction is one of the most critical steps in hyperspectral classification. To address the limitations of conventional convolutional layers, we employ a deep matrix capsule architecture, which is particularly effective in preserving spatial–spectral hierarchies. Capsule networks capture pose and orientation relationships between features, ensuring that the extracted representations are more robust and interpretable compared to standard CNNs. The architecture is summarized in Table 3, based on a window size of 25 × 25 centered on each pixel of the Indian Pines dataset.

Table 3 describes the architecture of the proposed model, which begins with an initial convolutional layer to capture low-level spatial–spectral features. The extracted features are then passed to the primary capsule layer, where they are transformed into matrix-based representations. Next, stacked convolutional capsule layers progressively learn higher-level spatial–spectral dependencies, allowing for more abstract and robust feature encoding. Finally, the class capsule layer produces discriminative class-level representations for classification. This hierarchical capsule-based framework has been shown to achieve superior performance compared to conventional CNNs in hyperspectral feature learning (Ravikumar et al., 2022).

3.4. Classifier

In the proposed method for HSI classification, two classifiers are utilized. The first classifier applies the SoftMax function to the output activations derived from the class capsules, yielding the predicted classes. Additionally, the SVM algorithm is utilized as an alternative classifier. The SoftMax function is a type of activation function commonly used in neural computing. It transforms a vector of real numbers into a probability distribution. By producing output values in the range of 0 to 1, the SoftMax function ensures that the sum of the probabilities equals 1. This function proves particularly beneficial in multi-class models, offering probability for each class, with the target class having the highest probability. Widely utilized in the output layers of diverse deep learning architectures, the SoftMax function is a cornerstone in classification tasks (Nwankpa et al., 2018). In the proposed framework, an SVM classifier is utilized due to its renowned generalization capability and proven track record of achieving high accuracy on training datasets. This approach is firmly grounded in statistical learning theory and adheres to the principle of structural risk minimization. It involves the classifiers endeavor to identify an optimal separating hyperplane with the widest possible margin between classes. In doing so, it focuses on training samples positioned at the extremes of the class distribution, thus promoting robust classification (Hasan et al., 2019).

4. Experiments results and discussion

Two publicly available hyperspectral image datasets were employed for extensive testing to assess the efficacy of the classification models. Detailed descriptions of these datasets can be found in the initial part of Section 3. Following this, the experimental setup and performance metrics are elaborated upon in the first and second

Table 3
The architecture-deep matrix capsules with window size 25 × 25 the last layer is based on the Indian pines data set.

INPUT CONVOLUTION LAYER					
Layer ID	Input Shape	Kernel Size	Stride	Padding	Output Shape
conv1	25 × 25 × 30	5 × 5	2	2	13 × 13 × 64
PRIMARY CAPSULE LAYER (Primary Caps)					
Layer ID	Input Shape	Kernel Size	Stride	Padding	Output Shape
Pose	13 × 13 × 64	1 × 1	1	0	13 × 13 × 32 × 4 × 4
A	13 × 13 × 64	1 × 1	1	0	13 × 13 × 32
CONVOLUTION CAPSULE LAYER1 (ConvCaps-1)					
Layer ID	Input Shape	Kernel Size	Stride	Padding	Output Shape
Pose	13 × 13 × 32 × 4 × 4	3 × 3	2	0	6 × 6 × 16 × 4 × 4
A	13 × 13 × 32	3 × 3	2	0	6 × 6 × 16
CONVOLUTION CAPSULE LAYER2 (ConvCaps-2)					
Layer ID	Input Shape	Kernel Size	Stride	Padding	Output Shape
Pose	6 × 6 × 16 × 4 × 4	3 × 3	1	0	4 × 4 × 16 × 4 × 4
A	6 × 6 × 16	3 × 3	1	0	4 × 4 × 16
CLASS CAPSULE LAYER (Class Caps)					
Layer ID	Input Shape	Kernel Size	Stride	Padding	Output Shape
Pose	4 × 4 × 16 × 4 × 4	1 × 1	1	0	4 × 4 × 16
A	4 × 4 × 16	1 × 1	1	0	16

subsections, respectively. Subsequently, our investigations and the outcomes of each HSI dataset are outlined and reviewed in the third segment of this section.

4.1. Experimental setup

In this study, HSI selects the important band using the band selection method. All the images were resized to the same width and height, but the number of spectral bands was less than the original number of bands. Second, the deep matrix capsule model extracted the feature extraction from the image. Finally, there are two classifiers for the classification of the HSI. The hyperparameters for the proposed show in Table 4.

Table 4
Summary of the experimental setup and parameter configurations used in the proposed hyperspectral image classification framework.

Component	Details
Band Selection	Parameters $p_1 = 150$ and $p_2 = 70$
Regularization (λ)	0.01
Feature Extraction	Deep Matrix Capsule Network (four stages: Conv, Primary Caps, ConvCaps-1/2, Class Caps)
Regularization (λ)	0.01
Optimizer	ADAM (learning rate = 1e-3, $\beta_1 = 0.9$, $\beta_2 = 0.999$)
Batch Size	5
Epochs	50
Training Ratio	10 % Indian pines, 3 % Salinas-A
Experiment Repeats	10 (with random training sample selection, averaged results reported)
Implementation	Python 3
Execution Environment	Google Colab (Windows-based), T4 GPU, 12.7 GB RAM

The hyperspectral image is partitioned into multiple small images based on the spatial dimension, and samples within each small image are randomly selected. This approach guarantees that training samples are selected from all spatial regions, ensuring comprehensive coverage across the entire image shown in Fig. 6.

4.2. Performance measures

In this study, the proposed model for HSI classification is evaluated using three key metrics: average accuracy (AA), overall accuracy (OA), and the Kappa coefficient. These evaluation metrics are derived from classification outcomes, where true positives (TP) denote correctly identified positive samples and true negatives (TN) indicate correctly recognized negative samples. Conversely, false positives (FP) occur when negative samples are misclassified as positives, and false negatives (FN) arise when positive samples are incorrectly labeled as negatives. Together, these measures provide a comprehensive assessment of the model's performance and highlight potential areas of misclassification.

$$\text{Recall} = \frac{\text{TP}}{\text{TP} + \text{FN}} \tag{7}$$

Moreover, we utilize Recall, which evaluates the proportion of correctly predicted samples in the chosen positive class relative to all possible positive predictions.

AA is a metric that aggregates and averages the recall values of each class, providing an overall assessment of the classification effectiveness across all classes. It serves as a reliable measure to evaluate the classification performance of the models comprehensively.

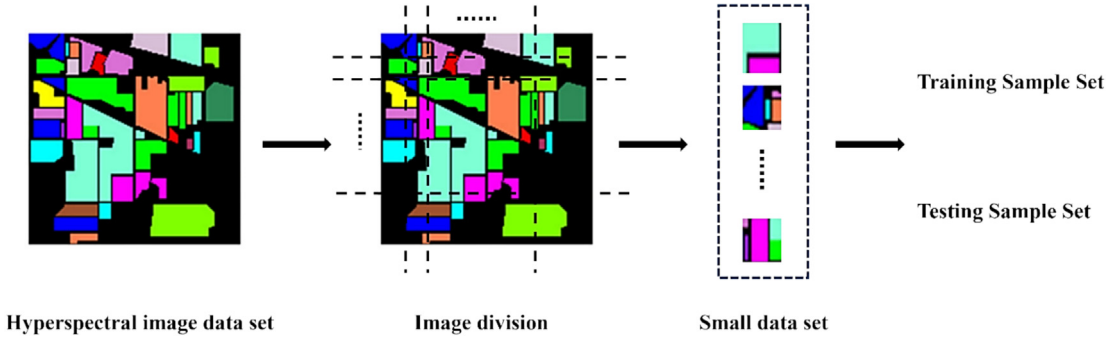

Fig. 6. The diagram shows a divided image to train the sample set and test the sample set.

$$AA = \frac{1}{n}\sum_{t=1}^{n} \text{Recall}_t \tag{8}$$

OA measures the proportion of correctly classified samples out of the total number of samples within a dataset.

$$OA = \frac{TP}{TP + FN + FP + TN} \tag{9}$$

Kappa coefficient is a measure of agreement between observed and predicted classifications, adjusting for agreement occurring by chance (Abdelhafez et al., 2024).

$$\text{Kappa} = \frac{2 \times (\text{TP} \times \text{TN} - \text{FN} \times \text{FP})}{(\text{TP} + \text{FP}) \times (\text{FP} + \text{TN}) + (\text{TP} + \text{FN}) \times (\text{FN} + \text{TN})} \tag{10}$$

These metrics offer a thorough evaluation of our models performance in HSI classification by addressing different facets of prediction accuracy and reliability.

4.3. Experimental results

In the following sections, we conduct extensive experiments using two publicly available hyperspectral datasets. These experiments are designed to assess the effectiveness of our proposed method against prominent band selection techniques, all within the same conditions and training ratios. To ensure reliability, we replicate the experimental setup five times, computing the mean of the results to evaluate the proposed methods efficacy. Accuracy comparison tables for each hyperspectral dataset are presented, showcasing that our proposed method consistently surpasses alternative band selection methods.

4.3.1. Classification results of the Indian Pines dataset

A performance comparison between the proposed band selection method and state-of-the-art methods on the Indian Pines dataset is detailed in Table 5. The AA is measured with training ratios (TR) of 5 % and 10 %, utilizing 70 band selections. Our method achieves AAs of 67.13 % and 73.64 %, respectively, outperforming all methods listed in the table. Compared with related methods reported in Table 5, the AAs of our model are approximately 3.76 % and 2.57 % higher than those of PCA, with TRs of 5 % and 10 %, respectively. For methods employing self-representation learning with sparse 1D-operational autoencoder (SRL-SOA) with a TR of 10 % and 70 band selections, such as SRL-SOA1, SRL-SOA3, and SRL-SOA5, their AAs were 72.90 %, 72.86 %, and 73.33 %, respectively. In contrast, the proposed model achieved a higher AA of 73.64 %. The AAs of our model are approximately 2.03 % and 0.63 % higher than those of graph-based probabilistic clustering band selection (GPCBS) (Hu et al.,

Table 5
Comparison of average accuracy on the Indian Pines dataset using different band selection methods with varying numbers of selected bands.

Method	Training Ratio (TR) 5 %			Training Ratio (TR) 10 %		
	Number of Band					
	50	60	70	50	60	70
PCA (Huang et al., 2023)	63.13 %	63.36 %	63.37 %	71.06 %	71.30 %	71.07 %
LDA (Li et al., 2018)	57.44 %	57.44 %	57.44 %	65.63 %	65.63 %	65.63 %
SVD (Sarker et al., 2020)	63.15 %	63.27 %	63.33 %	71.04 %	71.16 %	71.12 %
SpaBS (Li and Qi, 2011)	45.78 %	53.46 %	54.22 %	53.08 %	60.86 %	63.82 %
SRL-SOA1 (Ahishali et al., 2022)	66.61 %	64.61 %	66.31 %	71.86 %	72.82 %	72.90 %
SRL-SOA3 (Ahishali et al., 2022)	65.29 %	65.11 %	66.12 %	72.18 %	72.63 %	72.86 %
SRL-SOA5 (Ahishali et al., 2022)	66.42 %	65.26 %	66.18 %	71.19 %	72.19 %	73.33 %
GPCBS (Hu et al., 2025)	64.84 %	65.98 %	64.99 %	72.48 %	73.07 %	73.10 %
Proposed Method	**66.87 %**	**66.72 %**	**67.13 %**	**73.11 %**	**73.37 %**	**73.64 %**

Table 6
Comparison between the proposed method and other classification methods with the Indian Pines dataset.

Class	Method					
	Deep Matrix Capsules	HybridFCTCN	AMM-Net	DESSA-Net	Sentinel-2	Proposed
1	51.52	43.90	58.54	78.05	**100**	97.44
2	91.93	72.46	70.82	89.34	95.10	**99.03**
3	90.30	65.63	74.70	85.94	80.72	**96.62**
4	88.24	63.38	77.00	86.38	91.66	**92.10**
5	93.10	86.07	78.85	93.79	**97.95**	97.64
6	98.48	98.92	95.59	99.85	**100**	96.51
7	10.00	18.52	64.00	32.00	**100**	99.17
8	99.71	96.20	98.84	98.37	**100**	**100**
9	21.43	33.33	00.00	38.89	**100**	**100**
10	88.00	77.44	77.49	93.83	87.75	**94.34**
11	95.31	84.48	83.79	95.88	93.49	**99.00**
12	85.48	65.31	56.37	91.39	95.00	**95.69**
13	96.62	98.33	93.51	**100**	**100**	99.43
14	99.34	95.32	98.33	97.19	96.06	**99.36**
15	93.17	46.29	40.92	89.05	92.30	**96.55**
16	73.13	65.56	91.67	**100**	**100**	99.75
OA	93.01	80.11	80.33	93.45	93.69	**95.66**
AA	93.66	69.45	72.53	85.62	95.62	**97.66**
Kappa	92.02	74.79	77.52	92.52	92.82	**95.04**

2025), with TRs of 5 % and 10 % with 50 band selection, respectively.

To evaluate the effectiveness of the proposed approach, we compared it with several established classification methods, including deep matrix capsules (Ravikumar et al., 2022), HybridFCTCN (Li et al., 2023), AMM-Net (Wang et al., 2023), DESSA-Net (Mahmoodi et al., 2024), and Sentinel-2 (Sharifi and Safari, 2025). Table 6 and Table 8 present the detailed classification results for each class, along with AA, OA, and kappa values across all methods on the two datasets. The comparative evaluation demonstrates that the proposed method consistently surpasses existing approaches, achieving higher classification accuracy. As reported in Table 6, it outperforms the Sentinel-2 baseline by 1.97 % in OA, 2.04 % in AA, and 2.22 % in the Kappa score on the Indian Pines dataset with a 10 % training ratio and 70 selected bands. While Sentinel-2 can approximate hyperspectral analysis, its limited number of bands, broad bandwidths, and missing spectral details reduce its effectiveness for precise classification, material identification, and spectral unmixing compared to true hyperspectral sensors. Furthermore, the proposed method secures the best results in 62.5 % of the classes, underscoring its clear advantage over the other evaluated techniques on the same dataset. Fig. 7 presents the confusion matrix

Table 7
Comparison of average accuracy on the Salinas-A dataset using different band selection methods with varying numbers of selected bands using TR (1%).

Method	Number of Band		
	50	60	70
PCA (Huang et al., 2023)	92.00 %	92.00 %	91.99 %
LDA (Li et al., 2018)	93.07 %	93.07 %	93.07 %
SVD (Sarker et al., 2020)	92.22 %	92.21 %	92.21 %
SpaBS (Li and Qi, 2011)	88.48 %	91.73 %	92.75 %
SRL-SOA1 (Ahishali et al., 2022)	92.42 %	91.67 %	90.89 %
SRL-SOA3 (Ahishali et al., 2022)	93.00 %	91.65 %	93.53 %
SRL-SOA5 (Ahishali et al., 2022)	92.86 %	93.19 %	92.92 %
GPCBS (Hu et al., 2025)	92.30 %	92.08 %	91.57 %
Proposed Method	**93.62 %**	**93.62 %**	**93.65 %**

Table 8
Comparison between the proposed method and other classification methods with the Salinas-A dataset.

Class	Method					
	Deep Matrix Capsules	HybridFCTCN	AMM-Net	DESSA-Net	Sentinel-2	Proposed
1	97.54	99.48	99.48	90.51	**99.74**	93.59
2	98.98	97.89	87.82	92.68	92.35	**99.59**
3	82.18	87.05	88.85	93.65	95.58	**97.66**
4	98.83	**100**	**100**	99.41	95.37	99.91
5	92.26	85.07	97.60	**100**	96.86	95.26
6	98.62	97.98	97.72	99.62	98.23	**99.68**
OA	95.21	95.75	94.98	96.51	95.57	**96.73**
AA	95.70	94.58	95.25	95.98	96.36	**97.91**
Kappa	94.96	94.66	93.71	95.64	94.47	**95.90**

obtained from the classification results of the proposed model on the Indian Pines dataset with a TR of 10 %. The dataset contains 16 land-cover classes, including alfalfa, corn (not-tilled), corn (min-tilled), corn, grass-pasture, grass-trees, grass-pasture-mowed, hay-windrowed, oats, soybean (not-tilled), soybean (min-tilled), soybean (clean), woods, buildings, grass-trees-drives, and stone-steel-towers. As illustrated, most classes achieved high accuracies, with most values concentrated along the diagonal. Minor misclassifications are observed in spectrally similar classes, such as different categories of corn and soybeans. Overall, the results demonstrate that the proposed model effectively captures the spectral–spatial characteristics of the dataset and achieves superior classification performance compared to related approaches.

4.3.2. Classification results of the Salinas-A dataset

The Salinas-A dataset was employed to further assess the proposed method. As presented in Table 7, the suggested approach achieved the highest performance, reach-

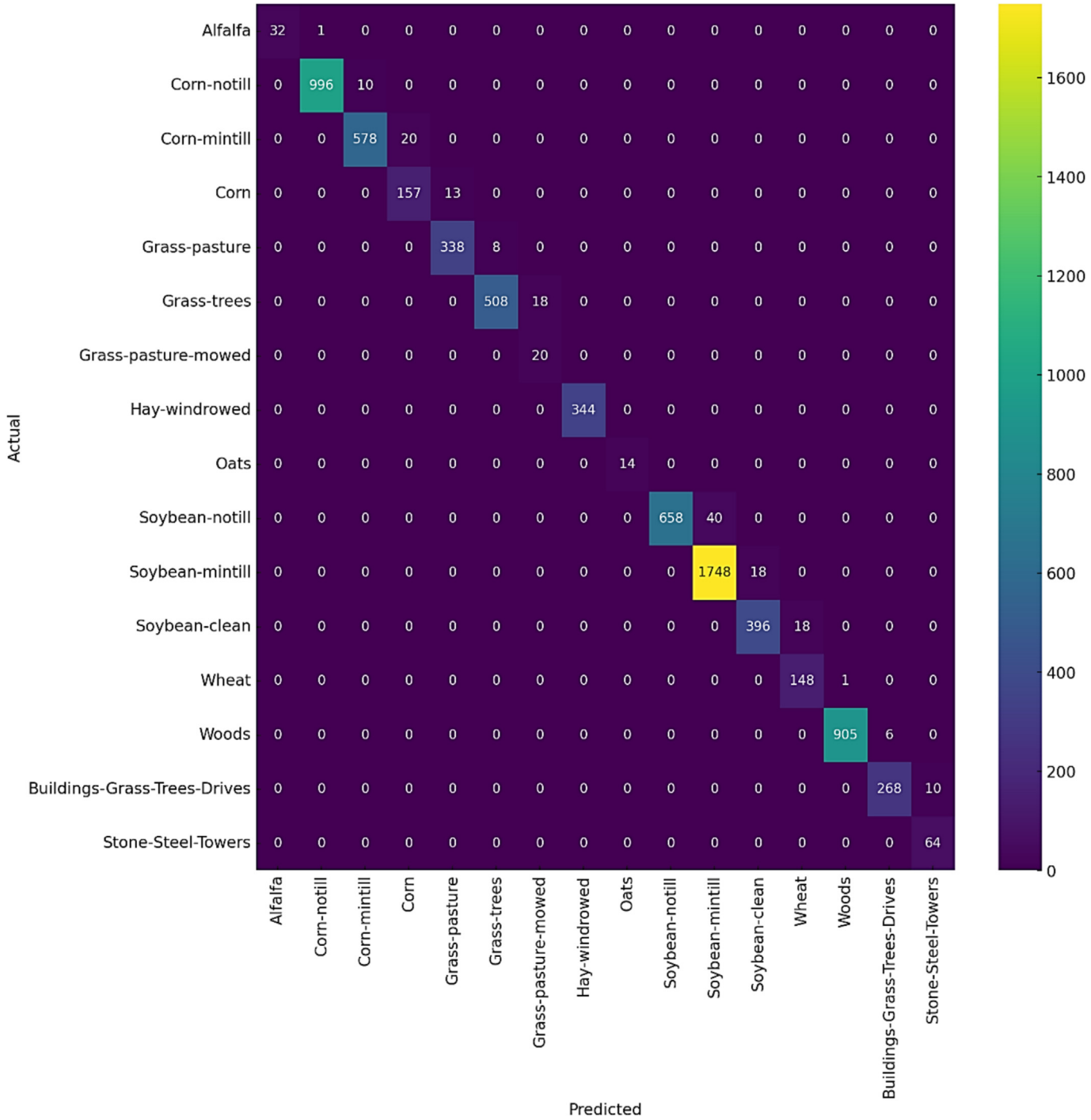

Fig. 7. The confusion matrix of the proposed model on the Indian Pines dataset (TR = 10 %).

ing 93.65 % average accuracy with a 1 % training ratio and 70 selected bands, outperforming all other compared methods. Specifically, our model exceeded GPCBS by approximately 1.58 % and 2.12 % when selecting 60 and 70 bands, respectively. While GPCBS effectively reduces spectral redundancy by modelling graph-based band relationships, it is computationally intensive and sensitive to parameter settings, which may compromise stability. Moreover, it can overlook subtle spectral variations that are critical for fine-grained hyperspectral classification.

Table 8 compares the performance of the proposed method with other existing approaches. On the Salinas-A dataset, using a training ratio of 3 % and 70 selected bands, the proposed approach surpasses HybridFCTCN, AMM-Net, and Sentinel-2 by 0.98 %, 1.75 %, and 1.16 % in OA; 3.33 %, 2.66 %, and 1.55 % in AA; and 1.24 %, 2.19 %, and 1.43 % in the Kappa score, respectively. The HybridFCTCN method enhances spatial–spectral feature extraction but comes with limitations, including high computational cost, dependence on sufficient training data, and risk of overfitting on small hyperspectral datasets. Moreover, its complex architecture reduces interpretability, making it challenging to identify which spectral–spatial features drive classification outcomes. AMM-Net effectively captures multi-scale spectral–spatial features, but its complex attention modules lead to high computational cost and dependence on sufficient labeled data. Additionally, its limited interpretability makes it difficult to explain the classification outcomes in practical applications. Fig. 8 shows the confusion matrix of the proposed model on the Salinas-A dataset with a TR of 3 %, where most classes achieve near-perfect accuracy. Minor misclassifications occur mainly between spectrally similar classes such as Broccoli_1 vs. Broccoli_2 and Fallow vs. Fallow smooth.

4.3.3. Discussion

While each of the compared band selection techniques has demonstrated effectiveness, they also suffer from inherent drawbacks that limit their applicability to hyperspectral image analysis. PCA (Jolliffe, 2011) and SVD (Sarker et al., 2020) achieve significant dimensionality reduction but at the cost of spectral interpretability, as the transformed features are linear combinations of original bands and thus lose direct physical meaning. LDA (Li et al., 2018) improves class separability by exploiting label information, yet its reliance on linear assumptions and sensitivity to limited training samples make it less robust in complex or small-sample scenarios. SpaBS (Li and Qi, 2011) preserves band interpretability by considering spectral–spatial context, but its performance can degrade when spatial information is weak or noisy. Similarly, SRL-SOA (Ahishali et al., 2022) provides computational efficiency with lower polynomial degrees, but this comes at the expense of modelling more complex nonlinear relationships in hyperspec-

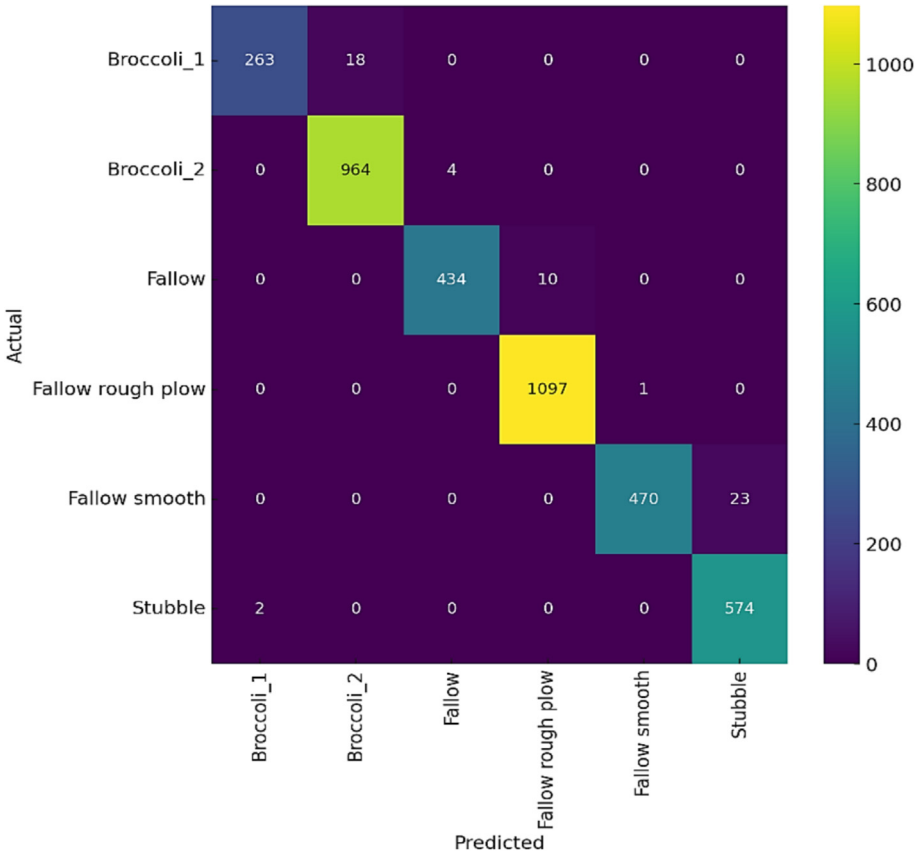

Fig. 8. The confusion matrix of the proposed model on the Salinas-A dataset (TR = 3 %).

tral data. GPCBS (Hu et al., 2025) mitigates redundancy by partitioning spectral space, yet the multi-stage clustering and forward selection process increases algorithmic complexity and may be sensitive to partition granularity. To address this challenge, the proposed framework achieves a balance between interpretability, efficiency, and robustness by integrating band selection with a hybrid CNN-SVM classifier. The band selection stage identifies the most informative spectral bands while suppressing noisy or redundant ones, thereby reducing dimensionality and improving data quality. For classification, CNN is employed to extract powerful spatial–spectral features; however, CNNs alone may suffer from overfitting, particularly when training samples are limited. In contrast, SVM is well-suited for high-dimensional data and provides strong generalization capability. By combining CNN-derived features with SVM, the framework leverages the strengths of both methods, enhancing robustness, lowering computational costs, and improving classification accuracy compared to using CNN or SVM individually. This hybrid strategy has been validated in several hyperspectral imaging studies (Chen et al., 2014, Li et al., 2016, Makantasis et al., 2015).

5. Conclusion

This study proposes a band selection method to enhance hyperspectral image (HSI) classification by identifying the most informative spectral bands. Combined with a deep matrix capsule model and classifier, the approach achieves superior accuracy, with 73.64 % and 97.66 % for Indian Pines and 93.65 % and 97.91 % for Salinas-A across two experimental settings. The method consistently outperforms competing band selection techniques in both accuracy and training efficiency. Beyond these results, the broader implication of this work lies in advancing efficient hyperspectral data analysis, which is critical for applications in agriculture, environmental monitoring, and land management. However, the model still faces computational limitations when dealing with very large-scale hyperspectral datasets, which may affect scalability and processing efficiency. Future research can address scalability by optimizing processing efficiency and integrating advanced architectures, such as transformer-based models, to further exploit spectral–spatial dependencies. Additionally, exploring compact feature representations and adaptive band selection strategies may yield more robust and generalizable solutions.

Data availability

The Indian Pines data that support the findings of this study are openly available at https://www.ehu.eus/ccwintco/index.php/Hyperspectral_Remote_Sensing_Scenes.

The Salinas-A data that support the findings of this study are openly available at https://www.ehu.eus/ccwintco/index.php/Hyperspectral_Remote_Sensing_Scenes.

Declaration of competing interest

The authors declare that they have no known competing financial interests or personal relationships that could have appeared to influence the work reported in this paper.

References

Abdelhafez, E.N., Hagag, A. Abassy, T.A. 2024. Feature extraction from hyperspectral images using RCNN and Vision Transformer. 2024 34th International Conference on Computer Theory and Applications (ICCTA), 2024. IEEE, pp. 213–219.

Ahishali, M., Kiranyaz, S., Ahmad, I. Gabbouj, M. 2022. SRL-SOA: self-representation learning with sparse 1D-operational autoencoder for hyperspectral image band selection. 2022 IEEE International Conference on Image Processing (ICIP). IEEE, 2296-2300.

Audebert, N., le Saux, B., Lefèvre, S., 2019. Deep learning for classification of hyperspectral data: a comparative review. IEEE Geosci. Remote Sens. Magaz. 7, 159–173.

Chen, Y., Lin, Z., Zhao, X., Wang, G., Gu, Y., 2014. Deep learning-based classification of hyperspectral data. IEEE J. Selected Topics Appl. Earth Observat. Remote Sens. 7, 2094–2107.

Eckel, L., Stütz, P., 2024. Hyperspectral sensor management for UAS: performance analysis of context-based system architectures for camouflage and UXO anomaly detection workflows. Drones 8, 529.

Hamida, A.B., Benoit, A., Lambert, P., Amar, C.B., 2018. 3-D deep learning approach for remote sensing image classification. IEEE Trans. Geosci. Remote Sens. 56, 4420–4434.

Hasan, H., Shafri, H.Z. Habshi, M. 2019. A comparison between support vector machine (SVM) and convolutional neural network (CNN) models for hyperspectral image classification. IOP Conference Series: Earth and Environmental Science, 2019. IOP Publishing, 012035.

Hu, T., Guo, X., Gao, P., 2025. Hyperspectral band selection method based on global partition clustering. Remote Sens. 17, 435.

Huang, L., Chen, Y., He, X., 2023. Spectral-spatial masked transformer with supervised and contrastive learning for hyperspectral image classification. IEEE Trans. Geosci. Remote Sens.

Jia, S., Jiang, S., Lin, Z., Li, N., Xu, M., Yu, S., 2021. A survey: deep learning for hyperspectral image classification with few labeled samples. Neurocomputing 448, 179–204.

Jolliffe, I., 2011. Principal component analysis. In: *International encyclopedia of statistical science*. Springer, Berlin, Heidelberg., pp. 1094–1096.

Li, H.-C., Lin, Z.-X., Ma, T.-Y., Zhao, X.-L., Plaza, A., Emery, W.J., 2023. Hybrid fully connected tensorized compression network for hyperspectral image classification. IEEE Trans. Geosci. Remote Sens. 61, 1–16.

Li, S., Qi, H. 2011. Sparse representation based band selection for hyperspectral images. In: 2011 18th IEEE International Conference on Image Processing, 2011. IEEE, pp. 2693-2696.

Li, T., Cai, Y., Cai, Z., Liu, X., Hu, Q., 2021. Nonlocal band attention network for hyperspectral image band selection. IEEE J. Selected Topics Appl. Earth Observat. Remote Sens. 14, 3462–3474.

Li, W., Feng, F., Li, H., Du, Q., 2018. Discriminant analysis-based dimension reduction for hyperspectral image classification: a survey of the most recent advances and an experimental comparison of different techniques. IEEE Geosci. Remote Sens. Magaz. 6, 15–34.

Li, W., Wu, G., Zhang, F., Du, Q., 2016. Hyperspectral image classification using deep pixel-pair features. IEEE Trans. Geosci. Remote Sens. 55, 844–853.

Lowe, A., Harrison, N., French, A.P., 2017. Hyperspectral image analysis techniques for the detection and classification of the early onset of plant disease and stress. Plant Methods 13, 80.

Lu, B., Dao, P.D., Liu, J., He, Y., Shang, J., 2020. Recent advances of hyperspectral imaging technology and applications in agriculture. Remote Sens. 12, 2659.

Mahmoodi, J., Abbasi-Moghadam, D., Sharifi, A., Nezamabadi-Pour, H., Esmaeili, M., Vafaeinejad, A., 2024. Dessa-net model: Hyperspectral image classification using an entropy filter with spatial and spectral attention modules on deepnet. IEEE J. Selected Topics Appl. Earth Observat. Remote Sens. 17, 14588–14613.

Makantasis, K., Karantzalos, K., Doulamis, A. Doulamis, N. 2015. Deep supervised learning for hyperspectral data classification through convolutional neural networks. 2015 IEEE international geoscience and remote sensing symposium (IGARSS). IEEE, pp. 4959–4962.

Mishra, S.P., Sarkar, U., Taraphder, S., Datta, S., Swain, D., Saikhom, R., Panda, S., Laishram, M., 2017. Multivariate statistical data analysis-principal component analysis (PCA). Int. J. Livestock Res. 7, 60–78.

Mohammad, R.R., Hagag, A., El-Dahshan, E.-S.-A., Gaber, A.E., Yahia, A., 2024. PolSAR image classification based on TCN deep learning: a case study of greater Cairo. Int. J. Image Data Fusion 15, 214–231.

Mou, L., Saha, S., Hua, Y., Bovolo, F., Bruzzone, L., Zhu, X.X., 2021. Deep reinforcement learning for band selection in hyperspectral image classification. IEEE Transact. Geosci. Remote Sens. 60, 1–14.

Nwankpa, C., Ijomah, W., Gachagan, A. Marshall, S. 2018. Activation functions: Comparison of trends in practice and research for deep learning. arXiv preprint arXiv:1811.03378.

Patro, R.N., Subudhi, S., Biswal, P.K., Dell'Acqua, F., 2021. A review of unsupervised band selection techniques: Land cover classification for hyperspectral earth observation data. IEEE Geosci. Remote Sens. Magaz. 9, 72–111.

Ravikumar, A., Rohit, P., Nair, M.K. Bhatia, V. 2022. Hyperspectral image classification using deep matrix capsules. In: 2022 International Conference on Data Science, Agents & Artificial Intelligence (ICDSAAI), 2022. IEEE, pp. 1–7.

Sarker, Y., Fahim, S.R., Hosen, M.S., Sarker, S. K., Mondal, M.N.I. Das, S.K. 2020. Regularized singular value decomposition based multidimensional convolutional neural network for hyperspectral image classification. In: 2020 IEEE Region 10 Symposium (TENSYMP), IEEE, pp. 1502–1505.

Sharifi, A., Safari, M.M., 2025. Enhancing the spatial resolution of sentinel-2 images through super-resolution using transformer-based deep learning models. IEEE J. Selected Topics Appl. Earth Observat. Remote Sens.

Shawky, O.A., Hagag, A., El-Dahshan, E.-S.-A., Ismail, M.A., 2020. Remote sensing image scene classification using CNN-MLP with data augmentation. Optik 221, 165356.

Stuart, M.B., McGonigle, A.J., Willmott, J.R., 2019. Hyperspectral imaging in environmental monitoring: a review of recent developments and technological advances in compact field deployable systems. Sensors 19, 3071.

Sun, W., Du, Q., 2019. Hyperspectral band selection: a review. IEEE Geosci. Remote Sens. Magaz. 7, 118–139.

Torun, O., Yuksel, S.E., Erdem, E., Imamoglu, N., Erdem, A., 2024. Hyperspectral image denoising via self-modulating convolutional neural networks. Signal Proc. 214, 109248.

Vafaeinejad, A., Alimohammadi, N., Sharifi, A., Safari, M.M., 2025. Super-resolution AI-based approach for extracting agricultural cadastral maps: form and content validation. IEEE J. Selected Topics Appl. Earth Observat. Remote Sens.

Vairavan, C., Kamble, B., Durgude, G., Ingle, S.R., Pugazenthi, K., 2024. Hyperspectral imaging of soil and crop: a review. J. Experim. Agricult. Int. 46, 48–61.

Wang, J., Sun, J., Zhang, E., Zhang, T., Yu, K., Peng, J., 2023. Hyperspectral image classification via deep network with attention mechanism and multigroup strategy. Expert Syst. Appl. 224, 119904.

Wang, X., Liang, Z., 2023. Hybrid network model based on 3D convolutional neural network and scalable graph convolutional network for hyperspectral image classification. IET Image Proc. 17, 256–273.

Wang, Y., Liu, M., Yang, Y., Li, Z., Du, Q., Chen, Y., Li, F., Yang, H., 2021. Heterogeneous few-shot learning for hyperspectral image classification. IEEE Geosci. Remote Sens. Lett. 19, 1–5.

Zhao, J., Tian, S., Geiß, C., Wang, L., Zhong, Y., Taubenböck, H., 2020. Spectral-spatial classification integrating band selection for hyperspectral imagery with severe noise bands. IEEE J. Selected Topics Appl. Earth Observat. Remote Sens. 13, 1597–1609.

Zhao, J., Zhou, B., Wang, G., Ying, J., Liu, J., Chen, Q., 2022. Spectral camouflage characteristics and recognition ability of targets based on visible/near-infrared hyperspectral images. Photonics MDPI, 957.